

pubs.acs.org/NanoLett Letter

Impact of Asymmetric Microstructure on Ion Transport in $Ti_3C_2T_x$ Membranes

Kimberly Ventura-Martinez, Yaguang Zhu, Austin Booth, and Kelsey B. Hatzell*



Cite This: Nano Lett. 2024, 24, 13551-13557



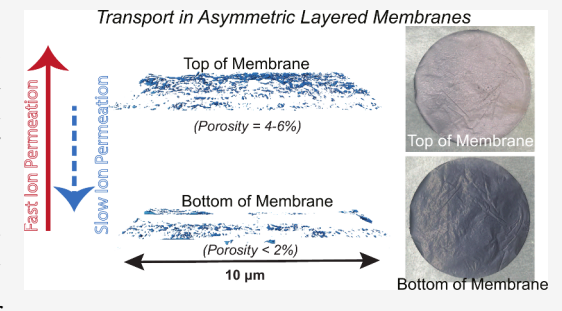
ACCESS

III Metrics & More

Article Recommendations

s Supporting Information

ABSTRACT: Consolidation or densification of low-dimensional MXene materials into membranes can result in the formation of asymmetric membrane structures. Nanostructural (short-range) and microstructural (long-range) heterogeneity can influence mass transport and separation mechanisms. Short-range structural dynamics include the presence of water confined between the 2D layers, while long-range structural properties include the formation of defects, micropores, and mesopores. Herein, it is demonstrated that structural heterogeneity in ${\rm Ti}_3{\rm C}_2{\rm T}_x$ membranes fabricated via vacuum-assisted filtration significantly affects ion transport. Higher ion permeabilities are achieved when the dense "bottom" side of the membrane, rather than the porous "top" side, faces the feed solution. Characterization of



the membrane reveals distinct differences in flake alignment, surface roughness, and porosity across the membrane. The directional dependence on permeability suggests that one region of the membrane experiences stronger internal concentration polarization, potentially suppressing permeability through the porous side of the membrane.

KEYWORDS: MXene, membrane heterogeneity, separations, water

Reclamation, extraction, and separation of valuable metals such as copper and nickel from industrial wastewater and lithium, vanadium, indium, boron, and rubidium from brines and seawater represents a powerful pathway for addressing a range of critical material challenges and reducing reliance on energy intensive mining processes. 1-3 Selective separations from complex mixtures can be challenging in applications related to wastewater or seawater because the solute of interest can occur at low concentrations or the waste stream can be highly caustic.^{4,5} Conventional polymer membranes are less effective under these conditions. Inorganic and ceramic membranes demonstrate resiliency at elevated temperatures and in caustic environments, but suffer from high costs associated with processing and manufacturing. 2,3,6 In addition, there are few classes of inorganic materials which can be processed into membranes (e.g., Al₂O₃, SiO₂, ZrO₂, TiO₂) due to the brittle nature of these materials. The discovery of lowdimensional transition metal carbide and nitride materials, known as MXene materials, has expanded the material palette for inorganic membranes and enables potential pathways for overcoming processing and mechanical challenges often associated with inorganic materials.^{3,7–9}

Transition metal carbides, carbonitrides, and nitrides, or MXenes, represent a large family of 2D materials derived from a class of ternary ceramic materials known as MAX. MAX phases are described by the general formula $M_{n+1}AX_n$, where $n = 1-4^{10}$ and M represents an early transition metal, A is a group A element (mostly groups 13 and 14), 11 and X is carbon and/or nitrogen. 12 Chemical processing of MAX phase

materials can result in the selective etching of A-layer elements. Exfoliation of high aspect ratio $M_{n+1}X_nT_x$ layers, where T_x represents the surface terminations (e.g., hydroxyl, oxygen, fluorine), $^{13-15}$ results in the formation of transition metal carbide or nitride 2D and/or low-dimensional materials. As layers stack, the spacing between them, influenced by surface terminations and intercalated species, leads to the formation of sub-nanochannels within the MXene structure. These interlayer spacings are a critical feature, providing pathways for ion transport, making MXenes particularly attractive for applications such as energy storage, water purification, and gas separation. 13

In 2015, Ren et al. reported the charge- and size-selective permeation of a group of cations through ${\rm Ti_3C_2T_{xr}}$ pioneering its use as a separation membrane. Since then, a growing body of research has expanded on this foundation, exploring various separation applications and synthetic approaches for MXene membranes. These studies have investigated composite formation, 17–19 intercalation effects, 20,21 surface charge, 22,23 and various other factors influencing MXene membrane performance. 24–26 While many of these studies rely heavily

Received: June 29, 2024
Revised: October 11, 2024
Accepted: October 14, 2024

Published: October 17, 2024





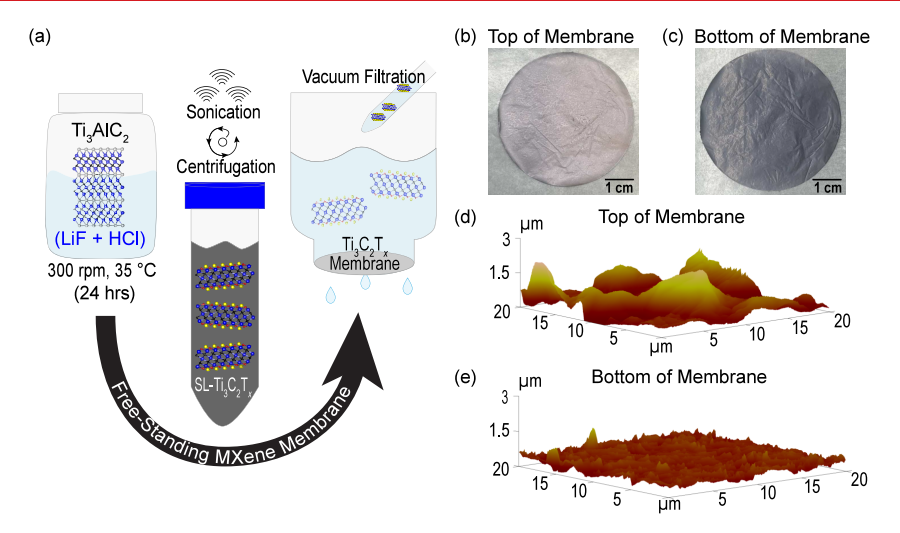


Figure 1. Solution processing of MXene materials from MAX and fabrication of MXene membranes using vacuum-assisted filtration techniques (a). Photograph of top side of membrane (b) and bottom side of membrane (c) after processing. Atomic force microscopy of surface roughness for the top side (d) and bottom side (e) of the membrane.

on vacuum-assisted filtration methods, which can result in variable consolidation, densification, and the formation of asymmetric membranes, the impact of these processing techniques on MXene membrane structure and performance has not been thoroughly explored. In other widely studied 2D membranes, such as graphene oxide and ${\rm MoS}_2$, variability resulting from vacuum filtration, including in flake alignment, have been observed to significantly impact membrane structure and performance. However, the effects induced by vacuum-assisted filtration on the overall structure and ion transport properties of ${\rm Ti}_3{\rm C}_2{\rm T}_x$ membranes remain largely unexplored.

Molecular and ion transport is critical in applications like batteries,³² colloid science,³³ biological applications,³⁴ and separations,^{35,36} all of which rely on ion mobility in confined regions where pore sizes are comparable to the Debye screening length. 5,37,38 At these dimensions, biophysicists have observed efficient transport and selectivity mechanisms.³⁴ Recent advancements in ion permeation have highlighted the role of nanochannels in controlling ion selectivity and transport rates, particularly in engineered materials like synthetic membranes and nanofluidic devices. 16,39,40 Studies have shown that the structure and chemistry of these channels can be precisely tuned to enhance ion conductivity and selectivity, leading to significant improvements in energy storage systems and water purification technologies. 41-4 Specifically, recent studies have identified Al3+20 sodium alginate, 25 and ethanol45 as potent agents to lock the nanochannel size to decrease ion permeabilities. However, the transport of water and ions through structurally heterogeneous materials like electrodes and membranes, which combine small-scale domains (e.g., 1-10 nm 'single digit nanochannels') with macroporous regions, 38,46 is still not completely understood. Understanding how structural heterogeneity, such as variations in pore distribution and interlayer spacings, affects transport is key to optimizing MXene membranes and other advanced materials.

To directly explore how membrane structural heterogeneity impacts ionic transport, we prepared freestanding membranes from colloidal solutions of $Ti_3C_2T_x$ by using vacuum filtration (Figure 1a). Facilitated by vacuum, negatively charged MXene

flakes were deposited onto a polymeric Celgard 3501 substrate as water passed through, forming a laminar structure in which MXene layers are separated by nanometer-scale channels. Once the entire colloidal solution was filtered, a freestanding membrane (thickness within 2–5 μ m) was peeled off the substrate (Supporting Information, Materials and Methods).

The consolidation or densification of low-dimensional MXene materials into a membrane involves various physical and chemical mechanisms, affecting both the membrane's nanostructure (short-range) and microstructure (long-range). Short-range structural dynamics include the presence and concentration of water confined between the layers, while longrange structural properties include micropore size and distribution. Dynamics such as flake rearrangement, sliding, and pressure-driven fluid flow all contribute to the final membrane structure. Since membrane fabrication resembles a layer-by-layer growth process, the material closest to the substrate (i.e., bottom) interacts with a larger volume of water compared to the layer deposited near the end of filtration (i.e., top). Additionally, as the membrane thickens during filtration, the vacuum applied to the top may be reduced relative to the bottom, further influencing the structure. Recent research suggests that although water molecules act as a lubricant and enhance the sliding of 2D sheets, the structure may remain somewhat disordered until the water is removed.⁴⁷ Once the water is removed, the sheets can collapse and stabilize into a more ordered and densely packed structure. Thus, the top and bottom regions exhibit different stacking structures because of different drying conditions. Furthermore, variations in the local concentration in the MXene solution during filtration could lead to flake misalignment, as regions with higher solute concentrations may affect flake distribution and orientation. Since vacuum filtration is the most common method for fabricating 2D membranes, understanding the differences in densification between the sides of Ti₃C₂T_x membranes could have implications for other 2D materials processed using aqueous-based filtration.

Qualitatively, the impact of processing variability on membrane structure is evident from the color change between the top (Figure 1b) and bottom (Figure 1c) of the membrane. The top of the membrane has a metallic sheen, while the

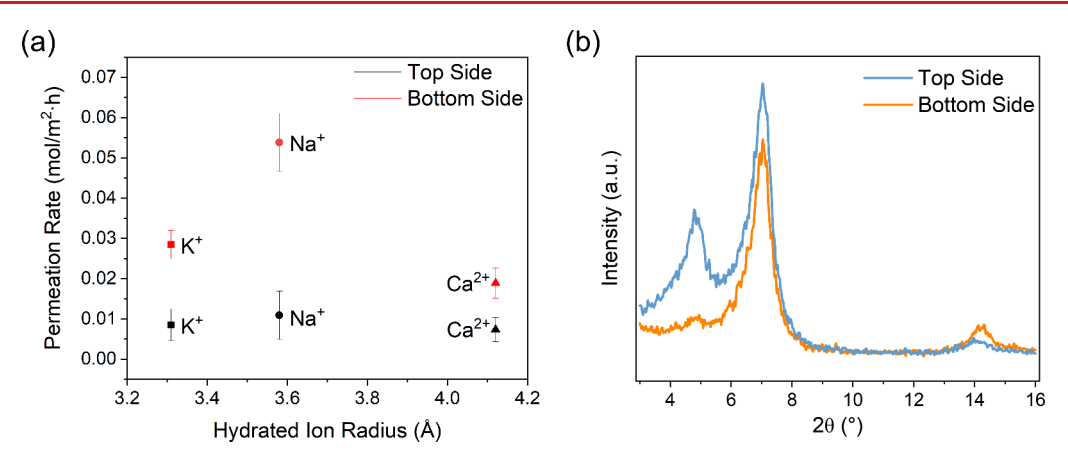


Figure 2. Permeation rates for different cations when the porous top of the membrane faces the feed and the dense bottom of the membrane faces the feed (a) and X-ray diffraction of interlayer dynamics (short-range structure) at top and bottom of the membrane (b).

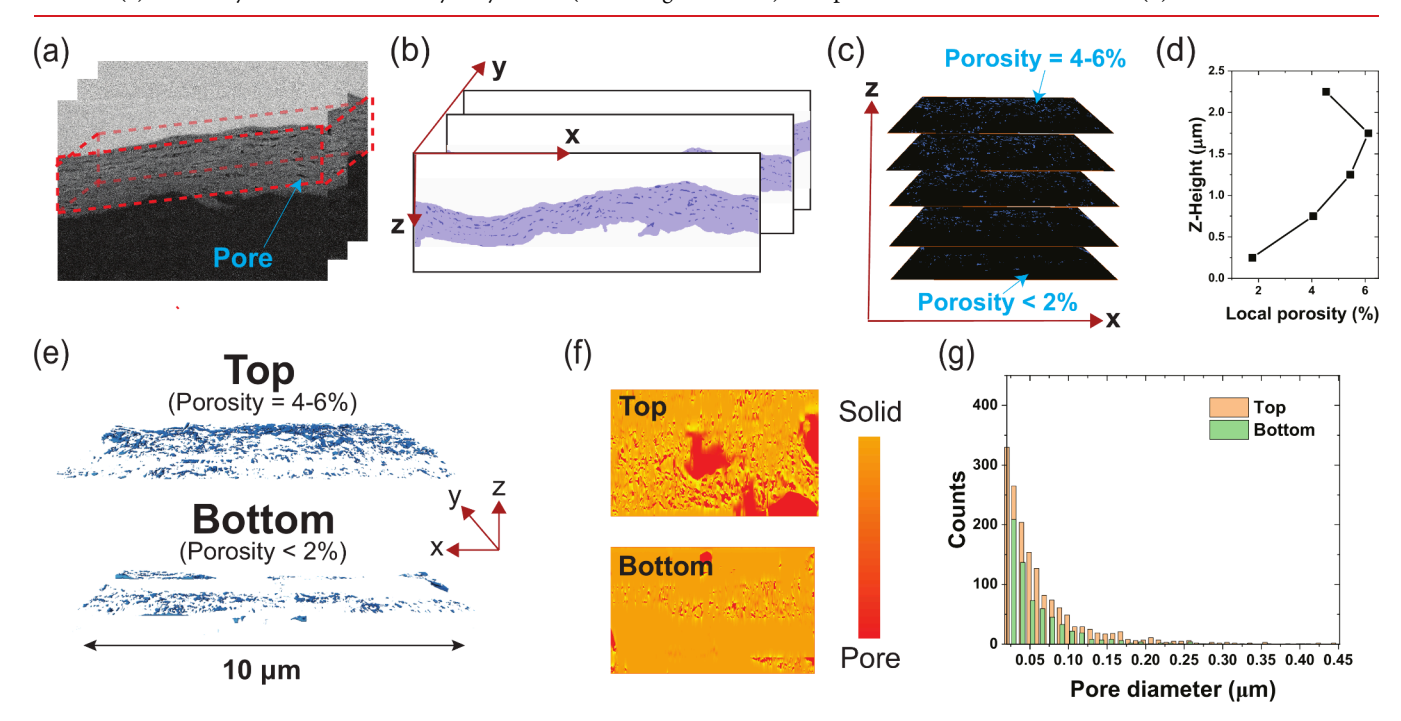


Figure 3. Scanning electron microscopy coupled with focused ion beam imaging of MXene membrane (a) and binarization revealing pores/defects and solid domain (b). Reconstructing image in the z-domain (c) reveals pore gradients in the membrane (d). 3-dimensional visualization of pores at top (porous) and bottom (dense) part of membrane (e) and heat map showing local heterogeneity of pores superimposed onto one z-layer (f). Pore size distribution in different regions of membrane (g).

bottom of the membrane appears a muted gray color. Quantitatively, AFM data reveals that the top side is significantly rougher, with R_a and $R_{\rm max}$ values of 398.5 nm and 3.1 μ m, respectively, compared to the bottom side's 101.1 nm and 1.6 μ m (Supporting Information, Table S1). This difference is further visualized in corresponding roughness plots (Figure 1d-e). Contrary to expectation, the metallic sheen is observed on the rougher surface (top), suggesting that the color difference may be due to the types of flakes within each microenvironment. Multilayer flakes, which contribute more to diffuse light scattering, likely settled at the bottom of the membrane during filtration, while larger, flat single-layer flakes comprise the top. Thus, despite its smoother surface, the bottom side's dull color may result from the diffuse light scattering caused by the larger presence of multilayer flakes.

Structural heterogeneity can impact water intrusion and water and ion permeability through the membrane. Ions can

only transport through channels that are sufficiently hydrated to facilitate diffusion.¹⁶ There are reports which suggest that ions can partially desolvate while transporting through confined regions of the membrane, but in general all ions will still require the presence of water for transport. Ion permeation measurements using an H-cell configuration were conducted to understand the implications of structural heterogeneity and directionality on transport (Supporting Information, Materials and Methods). Experiments were conducted with the top side (i.e., rough interface) facing the feed (black markers) and the bottom side (i.e., flat interface) facing the feed (red markers) (Figure 2a). The permeation rates of K⁺, Na⁺, and Ca²⁺ were 0.028, 0.054, and 0.017 mol m⁻²h⁻¹ (Figure 2a) when the bottom side (flat interface) was facing the feed. The permeation rates for each of these ions decreased by 3-5× when the top side (rough interface) was facing the feed. This shows that structural heterogeneity that

Nano Letters pubs.acs.org/NanoLett Letter

manifests during the consolidation and densification of the membrane influences transport mechanisms within the membrane. Additional studies were conducted to address the possibility that membrane thickness could have an effect on permeation rates (Supporting Information, (Figure S2)). Nevertheless, the findings continue to highlight a noticeable difference between the two sides of the membrane.

Short-range structural features (e.g., interlayer dynamics) can be probed using grazing-incidence X-ray diffraction (Figure 2b). The small incident angle of 0.5° allowed us to extract the d-spacing between MXene flakes at chemical microenvironments relevant to the top of the membrane (i.e., rough interface) and the bottom of the membrane (i.e., flat interface). A strong peak at 7° is observed at both interfaces, corresponding to a *d*-spacing of 1.26 nm. A second peak at 4.8° is evident at the top side of the membrane (rough interface), suggesting less aligned and more disordered MXene flakes as well as a slightly larger d-spacing of 1.84 nm. Larger d-spacing between the layers may be a sign of greater local water concentration at the top side of the membrane (rough interface), possibly due to a reduction in the vacuum-assisted filtration rate as the membrane thickness accumulates. The bottom of the MXene membrane only demonstrates a single peak at 7°, which suggests that there is more flake alignment (greater densification) at that interface. These results may support the suspected densification mechanism mentioned previously,⁴⁷ in which water removal becomes key to achieving dense, ordered structures, since the bottom may experience a larger vacuum during filtration. It is important to note that neither XRD spectrum alone is representative of an entire membrane. Instead, each membrane will have a top (larger dspacing) and bottom (smaller d-spacing) interface. Ions must always permeate through both regions of the membrane; the observed difference in transport behavior depends on whether ions encounter the top or bottom interface first.

Long-range structural features including pore size, pore size distribution, and pore connectivity through the thickness of the membrane can also influence permeation properties. Scanning electron microscopy (SEM) coupled with a focused ion beam (FIB) enable 3-D destructive imaging of the MXene membrane with resolutions around 7, 25, and 5 nm in x, y and z directions (Figure 3a). Structural features below this resolution cannot be captured via these direct imaging tools. Two-dimensional scanning electron microscopy images are taken of the membrane thickness, the FIB is used to mill away a prescribed thickness, and then another image is acquired. Binarization of the 2D images reveals the two discrete phases in the membrane (pores and solid inorganic phase). 48,49 Pores or sites with delaminated nanosheets are visible and can range from ~20 to ~450 nm; measures were implemented to ensure that these pores were not the result of FIB-induced defects (Supporting Information, Materials and Methods). These pores can lead to local hot-spots for preferential ion and water transport. In contrast, the nanochannels that separate the stacked MXene layers are around <2 nm, as measured using XRD. Ions transporting through the nanochannels may require partial desolvation of their hydration shell and thus have a higher activation energy barrier for mobility. Binarization of solid and pore phases through the thickness of the membrane (Figure 3c) reveals a porosity heterogeneity (Figure 3d). The porosity is highest near the top of the membrane (rough interface) and is lowest at the bottom (flat interface) of the membrane. The porosity increases from less than 2% at the

bottom to 4–6% at the top of the membrane (Figure 3d). Notably, the porosity does slightly decrease again at the very top surface of the membrane (z = 2.3 μ m). This may occur due to enhanced evaporation or other surface-specific processes which could improve flake stacking at the surface itself. Three-dimensional reconstruction of the pore regions at the top and bottom of the membrane (Figure 3e) demonstrates highly connected pores at the top of the membrane and discrete and unconnected pores at the bottom of the film.

The pores at the top and bottom of the film can be visualized in 3 dimensions after reconstruction of segmented binarized images (Figure 3e). 48,49 There is a higher density of larger pores at the top of the membrane than at the bottom of the membrane, which can be visualized through averaging the top slices and bottom slices and superimposing the local porosity onto a heat map (Figure 3f). The region in red is representative of regions with a higher density of pores, and the region in orange is representative of regions with a higher density of solid phases. The bottom is much more homogeneous, while the top of the membrane has a great level of structural heterogeneity. This is in agreement with the X-ray diffraction results, which indicate greater flake alignment (high densification) in the region at the bottom of the membrane and a lower degree of flake alignment (low densification) in the region at the top of the membrane. Variable densification is likely driven by the passage of water through the membrane during processing and its subsequent removal by vacuum.⁴⁷ The region at the bottom of the membrane experiences a stronger vacuum compared to the top of the membrane, due to its proximity to the vacuum source, which creates resistance for the vacuum reaching the top. This more extensive water removal from the membrane may force the flakes into stable alignment and decrease the average pore size at the bottom of the membrane (Figure 3g).

The variability observed in permeation rates is likely related to the asymmetric organization of pores in the low-dimensional MXene membrane. Concentration polarization can inhibit permeation rates due to local reduction in driving force across the membrane. Decreases in permeability are evident when the porous side of the membrane faces the concentrated feed solution. In this arrangement water will migrate from the dilute side (e.g., permeate) through the dense part of the membrane to the concentrated side of the membrane (feed). Water migration from the dilute to concentrated region will dilute salt trapped within the porous region of the membrane and/or will push salt back into the feed domain, reducing the driving force for diffusion.⁵⁰ This specific phenomenon is known as dilutive internal concentration polarization. Both internal and external concentration polarization can be tailored via processing and materials design strategies (e.g., surface terminating groups).

The change in driving force due to concentration polarization was estimated by applying the following equation for water flux with dilutive internal concentration polarization to the studied MXene membranes in NaCl solution:

$$J_{w} = A \left[\pi_{D,b} \exp(-J_{w}K) - \pi_{F,b} \exp\left(\frac{J_{w}}{k}\right) \right]$$
(1)

Here, J_{w} is water flux, A is the pure water permeability coefficient, K is the solute resistivity to diffusion, and k is the mass transfer coefficient. $\pi_{D,b}$ is the osmotic pressure of the concentrated ("draw") solution, and $\pi_{F,b}$ is the osmotic pressure of the dilute solution (termed "feed" in the forward

Nano Letters pubs.acs.org/NanoLett Letter

osmosis literature, but "permeate" in the above experiments). Since the salt concentration in the permeate side is negligible, $\pi_{F,b}$ is assumed to be 0, and eq 1 can be simplified as follows:

$$J_{w} = A\pi_{D,b} \exp(-J_{w}K) \tag{2}$$

The solute resistivity to diffusion, *K*, is specific to the layer of the membrane facing the concentrated solution. It can be calculated as

$$K = \frac{t\tau}{D\varepsilon} \tag{3}$$

where D is the diffusion coefficient of the solute, and t, τ , and ε are the thickness, tortuosity, and porosity of the layer facing the concentrated solution. The tortuosity and porosity of the top and bottom layers were calculated via analysis of the 3D FIB reconstruction, yielding $\tau_{top}=1.20$, $\tau_{bottom}=1.02$, $\varepsilon_{top}=4.54$, and $\varepsilon_{bottom}=1.77$. The thickness of each layer is estimated to be 500 nm, and D_{Na} in MXene was recently experimentally estimated as $1.0\times 10^{-12}~\text{m}^2/\text{s}.^{51}$ Applying these values to eq 3 yields $K_{top}=0.037~\text{h}~\text{L}^{-1}~\text{m}^{-2}$ and $K_{bottom}=0.080~\text{h}~\text{L}^{-1}~\text{m}^{-2}$.

The pure water permeability coefficient, A, was determined for 2.5- μ m membranes via dead-end filtration tests at 1 bar pressure. Using the measured $A = 32.6 \text{ L m}^{-2} \text{ h}^{-1} \text{ bar}^{-1}$, $\pi_{D,b} = 9.9 \text{ bar for } 0.2 \text{ M NaCl}$, and the above K_{top} and K_{bottom} values, eq 2 can be solved implicitly for J_w using both membrane configurations.

When the top (porous side) of the membrane faces the 0.2 M NaCl solution, the calculated water flux is approximately $J_{w,top} = 51 \text{ L m}^{-2} \text{ h}^{-1}$. When the bottom (dense side) of the membrane faces the 0.2 M NaCl solution, the calculated water flux is approximately $J_{w,bottom} = 30 \text{ L m}^{-2} \text{ h}^{-1}$. In other words, the amount of water flowing from the permeate side to the feed side increases by over 70% when the porous top of the membrane faces the feed. This corresponds to greater dilution of salt in the porous layer and a reduced driving force for salt diffusion. While this difference is an estimate and may not fully explain the decreased permeability when the top side faces the feed, the above calculations are a proof of concept that heterogeneous tortuosity and porosity may dramatically affect water and salt flux for different membrane configurations. The observed 3-5× difference in permeation rates may be further explained by the different actual thicknesses of the top and bottom layers, which could not be precisely determined using FIB and were not taken into account in these calculations.

Ultimately, designing membranes that achieve both high permeability and high selectivity is critical for the reclamation of valuable metals from complex waste streams. This work underscores the importance of long- and short-range structural heterogeneities on the transport properties of Ti₃C₂T_r membranes. Ion permeation results for K+, Na+, and Ca+ indicate that transport is faster when the bottom side of the membrane faces the feed solution, compared to the top side. Characterization of each region of the membrane (via AFM, GIXRD, FIB-SEM) revealed a smooth, dense, ordered bottom and a rough, porous, disordered top. A recently reported densification mechanism in van der Waal materials⁴⁷ may help explain the observed structural heterogeneity: During vacuum filtration, water moving through the membrane can act as a lubricant for nanosheets, facilitating their sliding and alignment; however, the structure may remain somewhat disordered until the water is removed.

Moreover, calculations using experimental tortuosity and porosity values in the context of internal concentration polarization revealed a dramatic effect on water and salt flux, highlighting the need to account for structural differences in MXene membranes. To further understand these dynamics, future work could include computational studies to model the effects of nanosheet alignment and water removal on membrane performance. Additionally, given the importance of oxidation stability for scaled-up applications, combining the structural heterogeneity observations reported here with emerging synthesis strategies - such as the addition of excess aluminum during the MAX phase synthesis 12 and increasing hydrophobic functional group densities on MXene⁵² - could significantly enhance the long-term stability of MXene membranes. Preliminary XPS results for the oxidation stability of our membranes (Supporting Information, Figure S3) indicate promising potential for the practical implementation of these membranes in scaled-up applications.

ASSOCIATED CONTENT

Supporting Information

The Supporting Information is available free of charge at https://pubs.acs.org/doi/10.1021/acs.nanolett.4c03080.

Materials and methods (synthesis of Ti_3AlC_2 MAX phase and $Ti_3C_2T_x$ solution, preparation of freestanding membranes, description of ion permeation experiments, and conditions for AFM, GIXRD, FIB-SEM, XPS), table of AFM surface roughness values, Na^+ permeation rates for membranes of different thicknesses, and XPS spectra (Ti 2p) to assess oxidation stability after permeation testing (PDF)

AUTHOR INFORMATION

Corresponding Author

Kelsey B. Hatzell — Andlinger Center for Energy and the Environment, Princeton, New Jersey 08540, United States; Department of Mechanical and Aerospace Engineering, Princeton University, Princeton, New Jersey 08540, United States; ◎ orcid.org/0000-0002-5222-7288; Email: kelsey.hatzell@princeton.edu

Authors

Kimberly Ventura-Martinez — Andlinger Center for Energy and the Environment, Princeton, New Jersey 08540, United States; Department of Chemistry, Princeton University, Princeton, New Jersey 08540, United States; orcid.org/0000-0003-0921-2774

Yaguang Zhu — Andlinger Center for Energy and the Environment, Princeton, New Jersey 08540, United States; orcid.org/0000-0002-1522-4491

Austin Booth – Andlinger Center for Energy and the Environment, Princeton, New Jersey 08540, United States; Department of Chemical and Biological Engineering, Princeton University, Princeton, New Jersey 08540, United States

Complete contact information is available at: https://pubs.acs.org/10.1021/acs.nanolett.4c03080

Notes

The authors declare no competing financial interest.

ACKNOWLEDGMENTS

This work was supported as part of the Advanced Materials for Energy-Water Systems (AMEWS) Center, an Energy Frontier Research Center funded by the U.S. Department of Energy, Office of Science, Basic Energy Sciences at Argonne National Laboratory under Contract No. DE-AC02-06CH11357. The authors acknowledge the use of Princeton's Imaging and Analysis Center (IAC), which is partially supported by the Princeton Center for Complex Materials (PCCM), a National Science Foundation (NSF) Materials Research Science and Engineering Center (MRSEC; DMR-2011750).

REFERENCES

- (1) Kazi, O. A.; Chen, W.; Eatman, J. G.; Gao, F.; Liu, Y.; Wang, Y.; Xia, Z.; Darling, S. B. Material design strategies for recovery of critical resources from water. *Adv. Mater.* **2023**, *35*, 2300913.
- (2) Wang, M.; Sadhukhan, T.; Lewis, N. H.; Wang, M.; He, X.; Yan, G.; Ying, D.; Hoenig, E.; Han, Y.; Peng, G.; Tiede, D. M.; Zhou, H.; Tokmakoff, A.; Schatz, G. C.; Liu, C.; et al. Anomalously enhanced ion transport and uptake in functionalized angstrom-scale two-dimensional channels. *Proc. Natl. Acad. Sci. U. S. A.* **2024**, *121*, No. e2313616121.
- (3) Zaman, W.; Matsumoto, R. A.; Thompson, M. W.; Liu, Y.-H.; Bootwala, Y.; Dixit, M. B.; Nemsak, S.; Crumlin, E.; Hatzell, M. C.; Cummings, P. T.; Hatzell, K. B. In situ investigation of water on MXene interfaces. *Proceedings of the National Academy of Sciences* 2021, 118, No. e2108325118.
- (4) Gao, F.; Chen, W.; Eatman, J. G.; Waldman, R. Z.; Zaluzec, N. J.; Dong, R.; Nealey, P. F.; Darling, S. B. Pushing the limits of size selectivity in nanoscale solute separations. *Nature Water* **2024**, *2*, 521–530.
- (5) Moreno, D.; Bootwala, Y.; Tsai, W.-Y.; Gao, Q.; Shen, F.; Balke, N.; Hatzell, K. B.; Hatzell, M. C. In situ electrochemical dilatometry of phosphate anion electrosorption. *Environmental Science & Technology Letters* **2018**, *5*, 745–749.
- (6) Liu, Y.; Xia, Z.; Wang, Y.; Rozyyev, V.; Kazi, O. A.; Gao, F.; Wang, D.; Lee, S. S.; Koritala, R.; Wen, J.; et al. Montmorillonite Membranes with Tunable Ion Transport by Controlling Interlayer Spacing. ACS Appl. Mater. Interfaces 2023, 15, 57144–57152.
- (7) Shuck, C. E.; Sarycheva, A.; Anayee, M.; Levitt, A.; Zhu, Y.; Uzun, S.; Balitskiy, V.; Zahorodna, V.; Gogotsi, O.; Gogotsi, Y. Scalable synthesis of Ti3C2Tx mxene. *Adv. Eng. Mater.* **2020**, *22*, 1–10.
- (8) Shuck, C. E.; Han, M.; Maleski, K.; Hantanasirisakul, K.; Kim, S. J.; Choi, J.; Reil, W. E.; Gogotsi, Y. Effect of Ti3AlC2MAX phase on structure and properties of resultant Ti3C2T x MXene. ACS Applied Nano Materials 2019, 2, 3368–3376.
- (9) Zheng, Y.; Cáceres González, R. A.; Hatzell, M. C.; Hatzell, K. B. Challenges and Roadmap for Solar-Thermal Desalination. *ACS ES&T Engineering* **2023**, *3*, 1055–1082.
- (10) Deysher, G.; Shuck, C. E.; Hantanasirisakul, K.; Frey, N. C.; Foucher, A. C.; Maleski, K.; Sarycheva, A.; Shenoy, V. B.; Stach, E. A.; Anasori, B.; Gogotsi, Y. Synthesis of Mo4VAlC4MAX Phase and Two-Dimensional Mo4VC4MXene with Five Atomic Layers of Transition Metals. ACS Nano 2020, 14, 204–217.
- (11) Sokol, M.; Natu, V.; Kota, S.; Barsoum, M. W. On the Chemical Diversity of the MAX Phases. *Trends in Chemistry* **2019**, *1*, 210–223.
- (12) Mathis, T. S.; Maleski, K.; Goad, A.; Sarycheva, A.; Anayee, M.; Foucher, A. C.; Hantanasirisakul, K.; Shuck, C. E.; Stach, E. A.; Gogotsi, Y. Modified MAX phase synthesis for environmentally stable and highly conductive Ti3C2MXene. ACS Nano 2021, 15, 6420–6429.
- (13) Naguib, M.; Mochalin, V. N.; Barsoum, M. W.; Gogotsi, Y. 25th anniversary article: MXenes: a new family of two-dimensional materials. *Adv. Mater.* **2014**, *26*, 992–1005.
- (14) Ghidiu, M.; Naguib, M.; Shi, C.; Mashtalir, O.; Pan, L.; Zhang, B.; Yang, J.; Gogotsi, Y.; Billinge, S.; Barsoum, M. Synthesis and characterization of two-dimensional Nb 4 C 3 (MXene). *Chem. Commun.* **2014**, *50*, 9517–9520.

- (15) Ling, Z.; Ren, C. E.; Zhao, M.-Q.; Yang, J.; Giammarco, J. M.; Qiu, J.; Barsoum, M. W.; Gogotsi, Y. Flexible and conductive MXene films and nanocomposites with high capacitance. *Proc. Natl. Acad. Sci. U. S. A.* **2014**, *111*, 16676–16681.
- (16) Ren, C. E.; Hatzell, K. B.; Alhabeb, M.; Ling, Z.; Mahmoud, K. A.; Gogotsi, Y. Charge-and size-selective ion sieving through Ti3C2T x MXene membranes. *journal of physical chemistry letters* **2015**, 6, 4026–4031.
- (17) Kang, K. M.; Kim, D. W.; Ren, C. E.; Cho, K. M.; Kim, S. J.; Choi, J. H.; Nam, Y. T.; Gogotsi, Y.; Jung, H. T. Selective Molecular Separation on Ti3C2Tx-Graphene Oxide Membranes during Pressure-Driven Filtration: Comparison with Graphene Oxide and MXenes. ACS Appl. Mater. Interfaces 2017, 9, 44687–44694.
- (18) Wu, X.; Ding, M.; Xu, H.; Yang, W.; Zhang, K.; Tian, H.; Wang, H.; Xie, Z. Scalable Ti3C2Tx MXene Interlayered Forward Osmosis Membranes for Enhanced Water Purification and Organic Solvent Recovery. ACS Nano 2020, 14, 9125–9135.
- (19) Pandey, R. P.; Rasool, K.; Madhavan, V. E.; Aissa, B.; Gogotsi, Y.; Mahmoud, K. A. Ultrahigh-flux and Fouling-resistant Membranes Based on Layered Silver/MXene (Ti3C2Tx) Nanosheets. *Journal of Materials Chemistry A* **2018**, *6*, 3522–3533.
- (20) Ding, L.; Li, L.; Liu, Y.; Wu, Y.; Lu, Z.; Deng, J.; Wei, Y.; Caro, J.; Wang, H. Effective Ion Sieving with Ti3C2Tx MXene Membranes for Production of Drinking Water from Seawater. *Nature Sustainability* **2020**, *3*, 296–302.
- (21) Ding, L.; Wei, Y.; Wang, Y.; Chen, H.; Caro, J.; Wang, H. A Two-Dimensional Lamellar Membrane: MXene Nanosheet Stacks. *Angew. Chem.* **2017**, *56*, 1825–1829.
- (22) Pandey, L.; Liang, W.; VahidMohammadi, A.; Zhang, T.; Gogotsi, Y.; Wanunu, M. Hydrophilicity and Surface Charge Modulation of Ti3C2Tx MXene based Membranes for Water Desalination. *RSC Adv.* **2024**, *14*, 21635–21643.
- (23) Zhang, L.; Kan, X.; Huang, T.; Lao, J.; Luo, K.; Gao, J.; Liu, X.; Sui, K.; Jiang, L. Electric Field Modulated Water Permeation through Laminar Ti3C2Tx MXene membrane. *Water Res.* **2022**, 219, 118598.
- (24) Lu, Z.; Wei, Y.; Deng, J.; Ding, L.; Li, Z. K.; Wang, H. Self-Crosslinked MXene (Ti3C2Tx) Membranes with Good Antiswelling Property for Monovalent Metal Ion Exclusion. *ACS Nano* **2019**, *13*, 10535–10544.
- (25) Wang, J.; Zhang, Z.; Zhu, J.; Tian, M.; Zheng, S.; Wang, F.; Wang, X.; Wang, L. Ion Sieving by a Two-dimensional Ti3C2Tx Alginate Lamellar Membrane with Stable Interlayer Spacing. *Nat. Commun.* **2020**, *11*, 1–10.
- (26) Ren, C. E.; Alhabeb, M.; Byles, B. W.; Zhao, M. Q.; Anasori, B.; Pomerantseva, E.; Mahmoud, K. A.; Gogotsi, Y. Voltage-gated Ions Sieving through 2D MXene Ti3C2Tx Membranes. ACS Applied Nano Materials 2018, 1, 3644–3652.
- (27) Dikin, D. A.; Stankovich, S.; Zimney, E. J.; Piner, R. D.; Dommett, G. H.; Evmenenko, G.; Nguyen, S. T.; Ruoff, R. S. Preparation and Characterization of Graphene Oxide Paper. *Nature* **2007**, *448*, 457–460.
- (28) Schneider, R.; Tandel, A. M.; Deng, E.; Correa, D. S.; Lin, H. Scalable Syntheis of Ultrathin MoS2Membranes for Dye. *Journal of Membrane Science Letters* **2023**, 3, 100058.
- (29) Tsou, C. H.; An, Q. F.; Lo, S. C.; De Guzman, M.; Hung, W. S.; Hu, C. C.; Lee, K. R.; Lai, J. Y. Effect of Microstructure of Graphene Oxide Fabricated through Different Self-assembly Techniques on 1-butanol Dehydration. *J. Membr. Sci.* **2015**, *477*, 93–100.
- (30) Cui, X.; Wu, X.; Zhang, J.; Wang, J.; Zhang, H.; Du, F.; Qu, L.; Cao, X.; Zhang, P. A Loosely Stacked Lamellar Membrane of Irregular MoS2 Flakes for Ultrahigh Water and Organics Permeation. *Journal of Materials Chemistry A* **2019**, *7*, 12698–12705.
- (31) Tang, B.; Zhang, L.; Li, R.; Wu, J.; Hedhili, M. N.; Wang, P. Are vacuum-filtered reduced graphene oxide membranes symmetric? *Nanoscale* **2016**, *8*, 1108–1116.
- (32) Chmiola, J.; Yushin, G.; Gogotsi, Y.; Portet, C.; Simon, P.; Taberna, P.-L. Anomalous increase in carbon capacitance at pore sizes less than 1 nm. *Science* **2006**, *313*, 1760–1763.

- (33) Biesheuvel, P. Thermodynamic cycle analysis for capacitive deionization. *J. Colloid Interface Sci.* **2009**, 332, 258–264.
- (34) Roux, B. Ion channels and ion selectivity. Essays in biochemistry 2017, 61, 201–209.
- (35) Werber, J. R.; Osuji, C. O.; Elimelech, M. Materials for next-generation desalination and water purification membranes. *Nature Reviews Materials* **2016**, *1*, 1–15.
- (36) Zhang, J.; Hatzell, K. B.; Hatzell, M. A combined heat and power driven membrane capacitive deionization system. *Environmental Science & Technology Letters* **2017**, *4*, 470–474.
- (37) Yao, Y.-C.; Taqieddin, A.; Alibakhshi, M. A.; Wanunu, M.; Aluru, N. R.; Noy, A. Strong Electroosmotic Coupling Dominates Ion Conductance of 1.5 nm Diameter Carbon Nanotube Porins. *ACS Nano* **2019**, *13*, 12851–12859.
- (38) Faucher, S.; Aluru, N.; Bazant, M. Z.; Blankschtein, D.; Brozena, A. H.; Cumings, J.; Pedro de Souza, J.; Elimelech, M.; Epsztein, R.; Fourkas, J. T.; et al. Critical knowledge gaps in mass transport through single-digit nanopores: a review and perspective. *J. Phys. Chem. C* 2019, 123, 21309–21326.
- (39) Fane, A. G.; Wang, R.; Hu, M. X. Synthetic Membranes for Water Purification: Status and Future. *Angew. Chem., Int. Ed.* **2015**, 54, 3368–3386.
- (40) Wang, L.; Boutilier, M. S.; Kidambi, P. R.; Jang, D.; Hadjiconstantinou, N. G.; Karnik, R. Fundamental transport mechanisms, fabrication and potential applications of nanoporous atomically thin membranes. *Nat. Nanotechnol.* **2017**, *12*, 509–522.
- (41) Joshi, R.; Carbone, P.; Wang, F.; Kravets, V.; Su, Y.; Grigorieva, I.; Wu, H.; Geim, A.; Nair, R. Precise and Ultrafast Molecular Sieving Through Graphene Oxide Membranes. *Science* **2014**, *343*, 752–754.
- (42) Zhang, H.; Hou, J.; Hu, Y.; Wang, P.; Ou, R.; Jiang, L.; Liu, J. Z.; Freeman, B. D.; Hill, A. J.; Wang, H. Ultrafast selective transport of alkali metal ions in metal organic frameworks with subnanometer pores. *Science Advances* **2018**, *4*, 1.
- (43) Razmjou, A.; Asadnia, M.; Hosseini, E.; Habibnejad Korayem, A.; Chen, V. Design principles of ion selective nanostructured membranes for the extraction of lithium ions. *Nat. Commun.* **2019**, *10*, 5793
- (44) Zhao, C.; Zhang, Y.; Jia, Y.; Li, B.; Tang, W.; Shang, C.; Mo, R.; Li, P.; Liu, S.; Zhang, S. Polyamide membranes with nanoscale ordered structure for fast permeation and highly selective ion-ion separation. *Nat. Commun.* 2023, 14, 1112.
- (45) Kang, Y.; Hu, T.; Wang, Y.; He, K.; Wang, Z.; Hora, Y.; Zhao, W.; Xu, R.; Chen, Y.; Xie, Z.; et al. Nanoconfinement enabled non-covalently decorated MXene membranes for ion-sieving. *Nat. Commun.* 2023, 14, 1–9.
- (46) Lin, K.; Lin, C.-Y.; Polster, J. W.; Chen, Y.; Siwy, Z. S. Charge Inversion and Calcium Gating in Mixtures of Ions in Nanopores. *J. Am. Chem. Soc.* **2020**, *142*, 2925–2934.
- (47) Zhu, J.; Li, F.; Hou, Y. Z.; Li, H.; Xu, D.; Tan, J.; Du, J.; Wang, S.; Liu, Z.; Wu, H. A.; Wang, F. C.; Su, Y.; Cheng, H. M. Near-room-temperature water-mediated densification of bulk van der Waals materials from their nanosheets. *Nat. Mater.* **2024**, *23*, 604–611.
- (48) Zheng, Y.; Hatzell, K. B. Ultrasparse view X-ray computed tomography for 4D imaging. ACS Appl. Mater. Interfaces 2023, 15, 35024–35033.
- (49) Dixit, M. B.; Moreno, D.; Xiao, X.; Hatzell, M. C.; Hatzell, K. B. Mapping charge percolation in flowable electrodes used in capacitive deionization. *ACS Materials Letters* **2019**, *1*, 71–76.
- (50) McCutcheon, J. R.; Elimelech, M. Influence of concentrative and dilutive internal concentration polarization on flux behavior in forward osmosis. *Journal of membrane science* **2006**, 284, 237–247.
- (51) Yadav, S.; Kurra, N. Diffusion kinetics of ionic charge carriers across $Ti_3C_2T_x$ MXene—aqueous electrochemical interfaces. *Energy Storage Materials* **2024**, *65*, 103094.
- (52) Zhou, C.; Wang, D.; Lagunas, F.; Atterberry, B.; Lei, M.; Hu, H.; Zhou, Z.; Filatov, A. S.; Jiang, D.-e.; Rossini, A. J. Hybrid organic—inorganic two-dimensional metal carbide MXenes with amido-and imido-terminated surfaces. *Nat. Chem.* **2023**, *15*, 1722–1729.